Interannual changes of the floating ice shelf of Petermann Gletscher, North Greenland, from 2000 to 2012

Andreas MÜNCHOW,[1] Laurie PADMAN,[2] Helen A. FRICKER[3]

[1]College of Earth, Ocean and Environment, University of Delaware, Newark, DE, USA
E-mail: muenchow@udel.edu
[2]Earth & Space Research (ESR), Corvallis, OR, USA
[3]Scripps Institution of Oceanography, University of California, San Diego, La Jolla, CA, USA

ABSTRACT. Petermann Gletscher, northwest Greenland, drains 4% of the Greenland ice sheet into Nares Strait. Its floating ice shelf retreated from 81 to 48 km in length during two large calving events in 2010 and 2012. We document changes in the three-dimensional ice-shelf structure from 2000 to 2012, using repeated tracks of airborne laser altimetry and ice radio-echo sounding, ICESat laser altimetry and MODIS visible imagery. The recent ice-shelf velocity, measured by tracking surface features between flights in 2010 and 2011, is $\sim$1.25 km a^{-1}, $\sim$15–30% faster than estimates made before 2010. The steady-state along-flow ice divergence represents 6.3 Gt a^{-1} mass loss through basal melting ($\sim$5 Gt a^{-1}) and surface melting and sublimation ($\sim$1.0 Gt a^{-1}). Airborne laser altimeter data reveal thinning, both along a thin central channel and on the thicker ambient ice shelf. From 2007 to 2010 the ice shelf thinned by $\sim$5 m a^{-1}, which represents a non-steady mass loss of $\sim$4.1 Gt a^{-1}. We suggest that thinning in the basal channels structurally weakened the ice shelf and may have played a role in the recent calving events.

KEYWORDS: remote sensing

INTRODUCTION

Greenland's tidewater glaciers are losing mass, through thinning and retreat, at an increasing rate (Joughin and others, 2010a; Howat and others, 2011; Bjørk and others, 2012). Over the past decade there has been a general clockwise progression of mass loss (Khan and others, 2010; Chen and others, 2011), with initial retreat in southeastern Greenland (Luckman and others, 2006; Howat and others, 2008) followed by loss in the southwest (Joughin and others, 2004) and, most recently, in northwest Greenland (Khan and others, 2010). In addition to this general trend, there is significant spatial and temporal variability of glacier mass budgets that does not always correlate with readily observed surface forcing (Howat and others, 2011; Moon and others, 2012). These observations support the view that the mass balance of tidewater glaciers is sensitive to the delivery of ocean heat to their submarine portion (Straneo and Heimbach, 2013).

Many marine-terminating glaciers in Greenland north of 78° N terminate in ice shelves, floating extensions of the glaciers extending up to several tens of kilometers into the adjacent fjords (Rignot and others, 2001). While most North Greenland ice shelves have been relatively stable, Academy Glacier and CH Ostenfeld Gletscher lost their floating ice shelves in the 1950s (Higgins, 1991) and in 2001 (Joughin and others, 2010b), respectively. Zachariæisstrøm separated from its slow-moving ice shelf in 2012/13 after two decades of retreat. Petermann Gletscher lost >40% of its ice-shelf area during two major calving events in 2010 and 2012 (Johnson and others, 2011; Nick and others, 2013). What remains of Greenland's ice shelves is threatened by a changing climate, because both regional air (Chylek and others, 2009) and ocean temperatures (Zweng and Münchow, 2006; Polyakov and others, 2010; Münchow and others, 2011) continue to increase, while Arctic sea-ice cover continues to decline (Stroeve and others, 2012). Based on

recent observations in Antarctica and Greenland, we expect that reduction in size due to thinning and/or calving of these ice shelves could cause accelerated dynamic loss of adjacent grounded ice, and consequent sea-level rise (Scambos and others, 2004; Holland and others, 2008; Nick and others, 2013).

In this paper we describe changes in Petermann Gletscher (hereafter denoted PG) in northwest Greenland from 2000 to 2012, after the second large calving event (Fig. 1), using a range of remote-sensing ice surface and bottom measurements. Opportunistic ocean surveys of Petermann Fjord in 2009 (Johnson and others, 2011) and 2012 motivated studies to determine whether the calvings were historically unusual (Falkner and others, 2011), if they could be related to ocean variability, and if loss of this portion of the ice shelf could lead to accelerated discharge of grounded ice from PG.

BACKGROUND ON PETERMANN GLETSCHER

PG drains $\sim$69 000 km^2 (Rignot and others, 2001) of the 1 710 000 km^2 Greenland ice sheet, i.e. $\sim$4%, into Petermann Fjord, which is $\sim$15–20 km wide and extends $\sim$90 km from PG's present grounding line (Fig. 1). PG terminates in an ice shelf that, over the historical record since 1876, has been $\sim$70–80 km long (Falkner and others, 2011). The average ice thickness, based on satellite altimetry and ice-penetrating radio-echo sounding, is $\sim$300 m, and the glacier is grounded at $\sim$600 m depth below sea level (Rignot and Steffen, 2008). The glacier bed deepens for another 20 km upstream and is below sea level for another $\sim$60 km inland (Rignot, 1998; Bamber and others, 2013).

PG moves steadily seaward at a reported average rate of between 0.95 km a^{-1} (Higgins, 1991) and 1.1 km a^{-1} (Rignot and Steffen, 2008), with a seasonal modulation of $\sim$0.1 km a^{-1} (Nick and others, 2012). The total annual discharge at the grounding line is 12 ± 1 Gt a^{-1} (Rignot and Steffen,
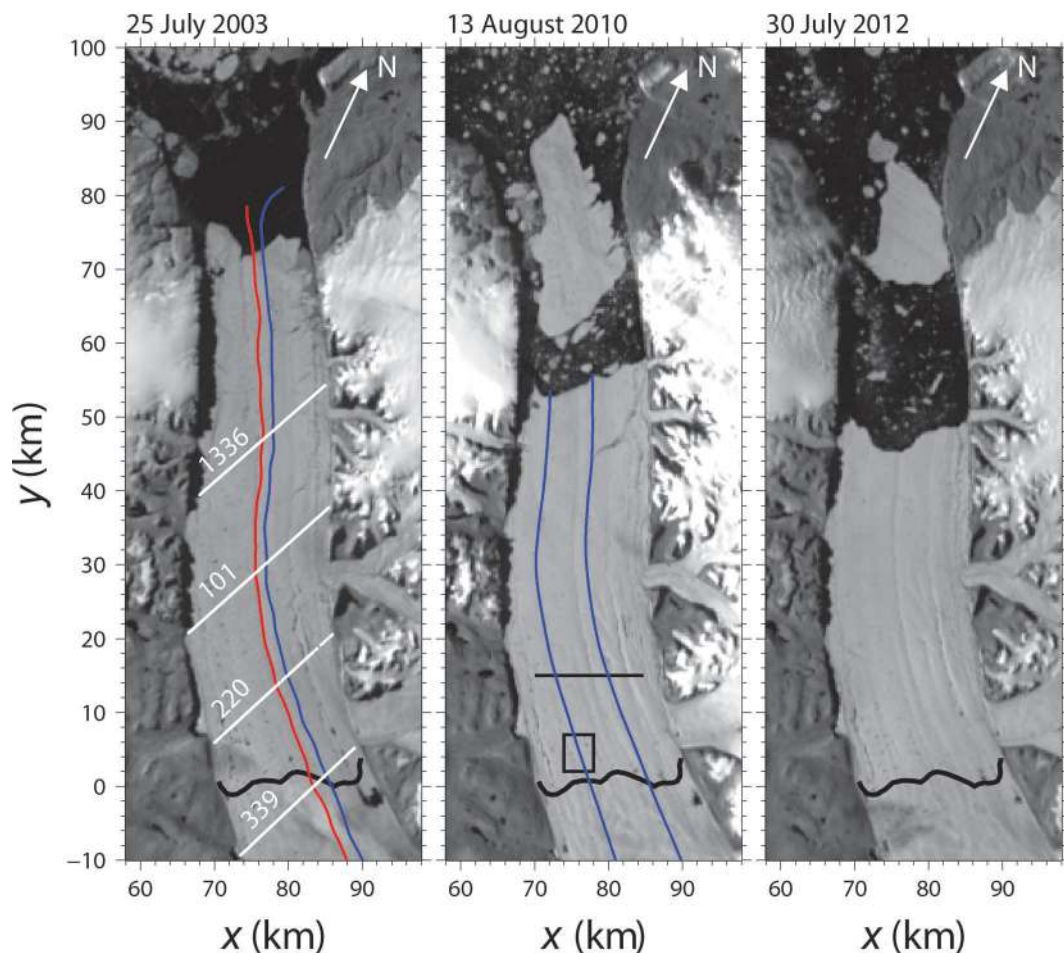
Fig. 1. MODIS images acquired over Petermann Gletscher on 25 July 2003 (left), 13 August 2010 (center) and 30 July 2012 (right). White lines on the left image are ICESat tracks, labeled by track number. Blue and red curves on the left panel are survey lines flown by NASA in 2002, 2003 and 2007. Blue curves in the center panel show the 2011 flight lines. Red indicates flight lines along the central channel, while blue marks flight lines along the ambient ice shelf. The thick black curve across the glacier near $y = 0$ km is the grounding-line location of Rignot and Steffen (2008). The horizontal black line near $y = 15$ km in the middle panel shows the location of MODIS surface reflectance profiles presented in Figure 6. The black rectangle shows an area of large and non-hydrostatic crevasses shown in Figure 10. Dark areas within 2 km of the western wall ($x \sim 70$ km) are shadows cast by high terrain, not ice-free water.

2008). Higgins (1991) estimated the long-term mean calving rate at $\sim 0.6\,\mathrm{Gt\,a^{-1}}$ or $\sim 5\%$ of the flux across the grounding line. Annual precipitation is small, and the ice-shelf surface undergoes net mass loss of $1.2\,\mathrm{m\,a^{-1}}$ ($1.0\,\mathrm{Gt\,a^{-1}}$ for an ice-shelf area of $900\,\mathrm{km^2}$ after the 2012 break-up) through winter sublimation and summer melting (Rignot and others, 2001; Rignot and Steffen, 2008). If the glacier is in a steady state, then $\sim 85\%$ of the mass loss must occur through basal melting. Sufficient ocean heat is available inside the fjord to melt the entire floating ice shelf, if the heat can flow into the sub-ice-shelf cavity (Johnson and others, 2011; Rignot and others, 2012). Hydrographic profiles below the ice shelf ~ 10 km seaward of the grounding line revealed water with temperature $T > 0°\mathrm{C}$ (Rignot and Steffen, 2008) at 600 m depth. This relatively warm ocean water originates from adjacent Nares Strait, which receives Arctic Atlantic Layer water from the Lincoln Sea in the Arctic Ocean (Münchow and others, 2007). Rignot and Steffen (2008) mapped the steady-state basal melt rate for the PG ice shelf, using satellite-derived divergence of ice flux. Values ranged from $\sim 30\,\mathrm{m\,a^{-1}}$ near the grounding line to $\sim 10\,\mathrm{m\,a^{-1}}$ closer to the ice front. Gladish and others (2012) developed a model of ice/ocean interactions that generated basal melt rates

ranging from $25\,\mathrm{m\,a^{-1}}$ at the grounding line to zero at the ice front.

The large calving events at PG in 2010 and 2012 reduced the ice-shelf length from 81 to 46 km (Figs 1 and 2). While PG has experienced large calving events in the past (Falkner and others, 2011), its terminus (ice front) has now retreated further back than has been observed since the first reported measurements in 1876 (Nares, 1876). By analogy with Jakobshavn Isbræ, Greenland (Holland and others, 2008; Motyka and others, 2011), we hypothesize that the observed slow warming of Atlantic-sourced waters in Nares Strait during the last decade (Münchow and others, 2011) could lead to increased basal melting of the PG ice shelf. We presently cannot determine if ocean warming in Nares Strait will continue, and modeling studies suggest that even complete loss of the PG ice shelf would not lead to accelerated loss of grounded ice (Nick and others, 2012, 2013). However, estimates of the PG ice-shelf mass budget provide a case study of the relationship between basal melting and ice-shelf retreat through calving, that is valuable for testing models used to describe coupling between ocean variability and glaciological response. It is now straightforward to track the areal extent of PG on short timescales (Johannessen and others, 2013). However, here we extend

that description to include how the ice thickness of PG has evolved over the last decade using repeat-track satellite and airborne altimetry and direct measurements of ice-thickness change using ice-penetrating radio-echo sounding.

DATA AND METHODS

Aircraft flight data

NASA conducted overflights of PG using DC-8 (2010) and P-3 (2002, 2003, 2007 and 2011) aircraft, the 2010 and 2011 flights being part of Operation IceBridge. The aircraft carried a multichannel ice-sounding radar (ISR) operated by the University of Kansas, to estimate the location of the air/ice and ice/ocean or ice/bedrock interfaces to determine ice thickness at ~100 m horizontal resolution (Gogineni and others, 2001). They also carried a scanning laser altimeter, the Airborne Topographic Mapper (ATM; Krabill and others, 2002). We used level 1B ATM data (Krabill, 2010) with spatial resolution of ~1 m. We applied a Lanczos low-pass filter to longitude, latitude and elevation, to generate an along-track series to represent features at scales greater than ~300 m, oversampled at ~30 m spacing. Two lines, separated across-fjord by ~1.5 km (Fig. 1), were repeated in multiple years. The western line followed a narrow surface channel while the eastern line was over thicker ice, that is more typical of the ice shelf.

Ice, Cloud and land Elevation Satellite (ICESat) data

We obtained elevation data from the Geoscience Laser Altimeter System (GLAS) on NASA's ICESat, which operated in campaign mode from October 2003 to November 2009 (Shuman and others, 2006). ICESat acquired elevation estimates every ~170 m along-track, with a footprint diameter of ~50–100 m (Abshire and others, 2005). Four ICESat tracks cross Petermann Fjord (Fig. 1) and, for each track, up to ten cloud-free repeats were acquired. Data processing followed protocols described by Padman and others (2008) and Fricker and others (2009). We used Release 633 of the GLA12 altimetry product, which we converted from the TOPEX/Poseidon reference ellipsoid to the WGS84 ellipsoid. We applied the GLA12 saturation correction (Fricker and others, 2005) and retided the elevations by adding back the GLA12 ocean tide corrections. Borsa and others (2013) reported a range error in the ICESat data, known as the Gaussian-centroid offset. We did not correct for this, however, since the amplitude of this offset is much smaller than our signal.
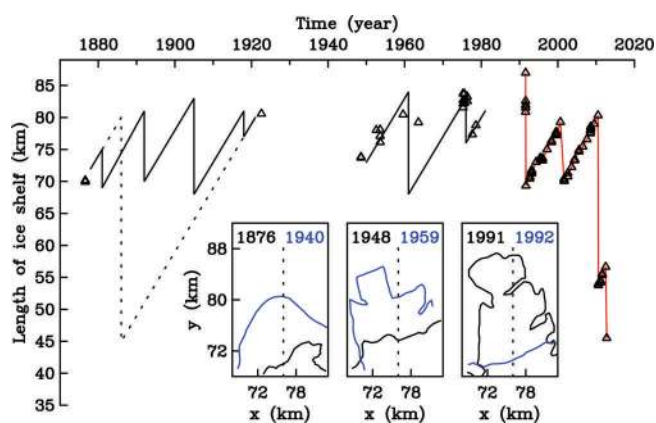

Fig. 2. Time series of the length of the ice shelf from 1876 to 2012. Selected shapes of the terminus are shown as insets (Falkner and others, 2011). Coordinates (x, y) for insets are the same as in Figure 1. Symbols indicate observations; dashed and solid time series show two alternate and hypothetical evolutions, with the slope indicating a 1 km a^{-1} advance of the terminus. Red line connects modern satellite data showing large calvings in 1991, 2001, 2010 and 2012.

Ice-sounding radar data

For the ice surface and bottom data from ISR, we removed an unknown platform bias by assuming hydrostatic equilibrium of a 30 km floating section of the ice shelf. The bias is assumed to be constant for each flight. Using an approach similar to Bindschadler and others (2011), we fitted estimates of ice thickness, H, from the ISR to

$$Z = \text{offset} + \text{ratio} \times H, \tag{1}$$

where Z is the ISR surface elevation above the geoid. The regression coefficients 'offset' and 'ratio' were determined via least-squares and represent, respectively, the unknown (constant per flight) platform offset and a buoyancy ratio. If the ice shelf is floating in hydrostatic equilibrium, then ratio $= (1 - \rho_{ice}/\rho_{water}) = 0.106$ for an ice density $\rho_{ice} = 917 \text{ kg m}^{-3}$ and an ocean density $\rho_{water} = 1026 \text{ kg m}^{-3}$. The offset includes an unknown firn/air correction (Bindschadler and others, 2011); however, this correction should be negligible for PG because annual snowfall is small compared with surface mass loss through melting and sublimation. Table 1 lists these regression coefficients along with pertinent details of aircraft surveys conducted over PG since 2002. The buoyancy ratio is close to the expected value for the ambient ice shelf, but deviates from hydrostatic for the central channel.
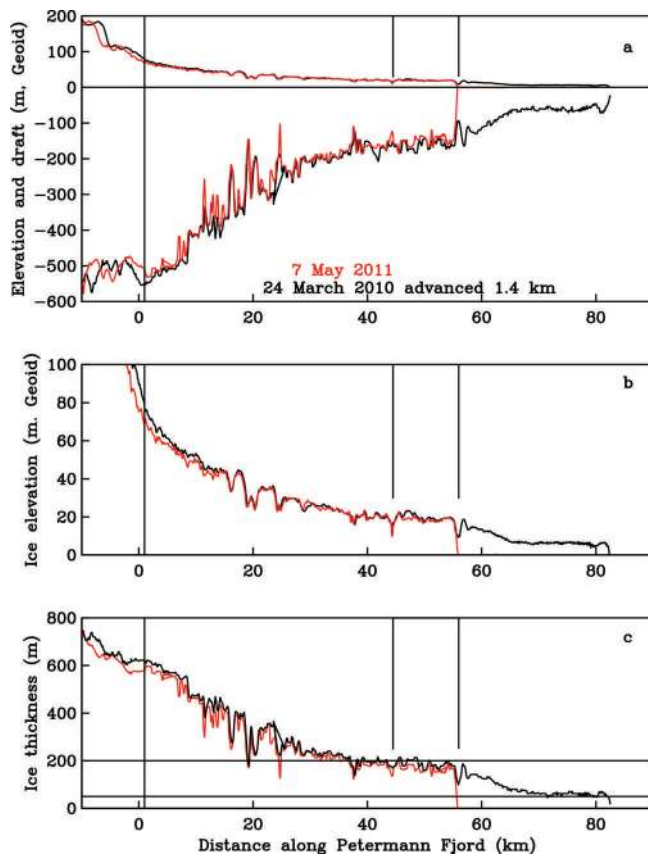
Table 1. Petermann Gletscher ISR data (date, across-channel location, x_i) and regression parameters of ISR ice thickness and ISR surface elevations (offset$_i$ and ratio$_i$) along the central channel ($i = 1$) and along the ambient ice shelf ($i = 2$) for profiling ISR and ATM sections. Listed parameters are determined from data along a common 30 km long segment of floating ice shelf, $y \in [21, 51]$ km (see Fig. 1 for locations). Tidal elevation estimates are for 81.25° N, 62° W (Padman and Erofeeva, 2004)

Date	x_1	offset$_1$	ratio$_1$	x_2	offset$_2$	ratio$_2$	Tide
	km	m		km	m		m
7 May 2011				77.47	−7.5	0.1065	0.08
24 Mar 2010	76.02	2.9	0.1658	77.51	6.9	0.1325	0.15
13 Sept 2007	76.08	532.4	0.1300	77.46	591.5	0.1154	0.15
14 May 2003	76.06	587.3	0.0800	77.48	574.8	0.0738	0.30
28 May 2002	76.06	−29.7	0.1159	77.47	−28.9	0.1007	0.13

Fig. 3. (a) Surface and basal elevation profiles along PG from the ATM and ISR for 7 May 2011 and 24 March 2010. (b, c) The ice surface elevation relative to EGM2008 geoid and ice thickness, respectively, revealing strong spatial correlation between years for a uniform $1.26\,\mathrm{km\,a^{-1}}$ advance of the glacier. The associated advection distance of $\sim 1.4\,\mathrm{km\,a^{-1}}$ has been applied to the 2010 data. The glacier is grounded near $y = 1\,\mathrm{km}$. The 2010 and 2012 break-up locations at $y = 56\,\mathrm{km}$ and $y = 44.5\,\mathrm{km}$ are indicated by vertical lines. Vertical bar at $y = 1\,\mathrm{km}$ indicates the grounding zone.

The ISR-based ice-thickness estimates are accurate to within 10 m (Gogineni and others, 2001), and the concurrent ATM estimates of the location of the ice surface (elevation) were accurate to $\sim 0.2\,\mathrm{m}$ (Krabill and others, 2002). We converted the ATM elevations to ice thickness assuming hydrostatic equilibrium, to estimate the location of the grounding line and to detect deviations from hydrostatic equilibrium (e.g. Fricker and others, 2002; Bindschadler and others, 2011).

No ice-penetrating ISR data are available concurrent with ICESat data; therefore, we cannot test the hydrostatic assumption for these cross-fjord transects.

Geoid and tidal corrections

We converted all ice elevation and draft data from the WGS-84 ellipsoid to the EGM2008 geoid (Pavlis and others, 2012) to estimate ice freeboard from surface elevation measurements. The freeboard allows us to estimate ice draft using the hydrostatic balance of the floating section of PG's ice shelf. We corrected all elevation data for tides using predictions from the AOTIM5 tide model (Padman and Erofeeva, 2004). This model does not resolve Petermann Fjord. Therefore, we used a model gridpoint at the entrance to the fjord rather than the actual locations of elevation measurements. We speculate that tidal variability inside the fjord is small, because the

barotropic tidal wave propagates in and out of the fjord within 10 min. Frictional forces under the floating ice shelf will change both tidal amplitude and propagation, but these are difficult to assess without a dynamical model or without knowledge of ocean current, bottom depth or ice-shelf topography. Reeh and others (2000) found tidal amplitudes under the 60 km long ice shelf of Nioghalvfjerdsfjorden off northeastern Greenland to vary <20% near the grounding line relative to the forcing open ocean tide; at PG, this variability would correspond to a tidal uncertainty of <0.1 m.

Moderate Resolution Imaging Spectroradiometer (MODIS) data

The MODIS flown aboard the Terra satellite provides radiation measurements starting in February 2000 at a spatial resolution of 250 m at nadir for the 865 nm spectral band. The polar orbiting, Sun-synchronous satellite has a repeat period of 16 days and provides ~ 8–12 scenes of northern Greenland each day. We used the raw Level-0 data distributed by NASA's Ocean Color Group along with altitude and ephemeris data. Following Luo and others (2008) and Trishchenko and others (2009), we converted these data to calibrated and geo-referenced 865 nm reflectance data. The subsequent gridding preserved the 250 m spatial resolution using a Green's function approach (Wessel, 2009) that also facilitated automated estimation of the reflectance gradient vector at each pixel. We constructed a time series of reflectance gradients from one cloud-free MODIS Terra image per year from 2000 to 2012, acquired within 135 min of 20:50 UTC between 30 April and 20 May of each year.

We made estimates of areal ice-shelf loss by manually counting MODIS pixels on paper, although there is uncertainty due to partial pixels and semi-detached areas of the ice island (Wang and Shi, 2009).

RESULTS

Changes in ice-shelf extent

The surface evolution of PG and the ice islands it calved are recorded by MODIS imagery from the summers of 2003, 2010 and 2012 (Fig. 1). During the 2003–10 period the glacier's terminus advanced $\sim 6\,\mathrm{km}$ (to $y \approx 80\,\mathrm{km}$; Fig. 1) even though, in 2008, two smaller calving events removed $30\,\mathrm{km^2}$ of ice shelf (not shown). The calving front shed $253 \pm 17\,\mathrm{km^2}$ on 4 August 2010; a further $130 \pm 10\,\mathrm{km^2}$ calved on 16 July 2012.

Figure 3 shows surface elevation from ATM and bottom topography from ISR for repeat airborne surveys on 24 March 2010 and 7 May 2011; $\delta t = 408$ days apart. The profile from 2010 has been shifted seaward by $\delta x = 1.4\,\mathrm{km}$ relative to the 2011 profile, to achieve the largest spatially lagged correlation between the two profiles for both surface elevation and ice thickness. This shift corresponds to an average ice flow rate of $V = \delta x / \delta t = 1.25 \pm 0.09\,\mathrm{km\,a^{-1}}$. The uncertainty is a 95% confidence limit or 1.96 times the standard error $\epsilon = 2\Delta / \sqrt{N}$, where $\Delta = 300\,\mathrm{m}$ and $N = 150$ represent, respectively, data spacing and degrees of freedom for the 45 km section of floating ice shelf used in the correlation. Our estimate of ice flow speed for the floating ice shelf is $\sim 30\%$ higher than those by Higgins (1991) for the late 20th century and Rignot and Steffen (2008) for 2002/03, but falls within the range of values given by Nick and others (2012) and Johannessen and others (2013) for the 2006–11 period.
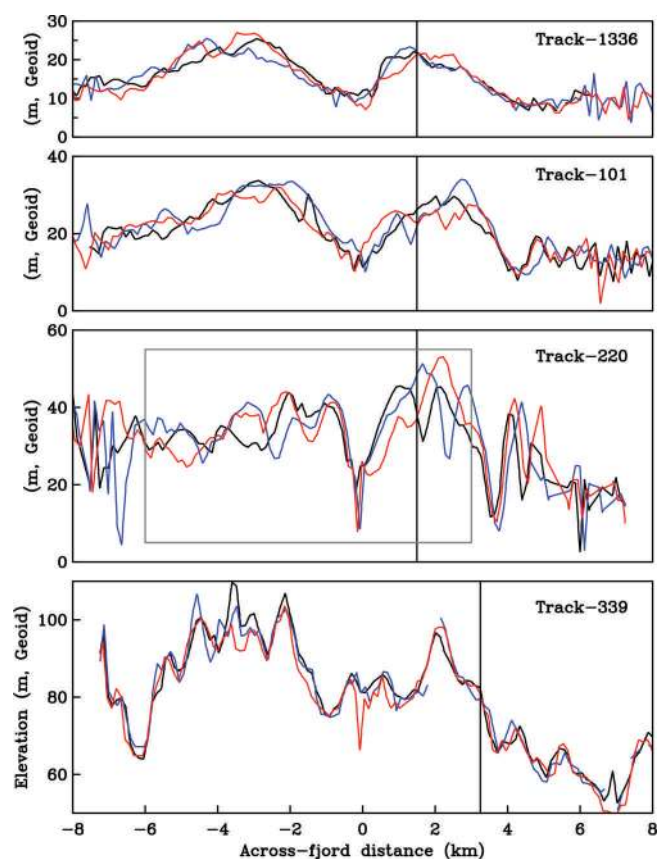
Fig. 4. ICESat-derived surface elevation profiles from selected repeat ICESat tracks across PG from north (track 1336, top) to south (track 339, bottom); Figure 1 shows the track locations. Black, blue and red indicate 2003, 2005 and 2007 (2008 for track 101) as the year of observation. Across-fjord distance is shifted for each track (but not year) so that $x' = 0$ indicates the time-averaged location of the central channel. Vertical lines indicate crossover location with airborne ATM track along the ambient ice shelf. The large boxed region for track 220 indicates data used to generate Figure 5.

The segments of the ice shelf that calved in 2010 and 2012 were, on average, 76 and 182 m thick (Fig. 3) with standard deviations of 6 and 16 m, respectively. Using these along-shelf profiles and assuming a realistic ice-thickness profile across the glacier (discussed below), we find that the mass loss during each of the two calving events in 2010 and 2012 was similar, $\sim 18 \pm 2$ Gt for each event.

After the 2012 calving event the terminus was at the most retreated of all locations in the historical record, which begins in 1876 (see fig. 1b of Falkner and others (2011), updated to the end of 2012 in our Fig. 2).

Elevation variability

The elevation of the PG ice shelf varies substantially on scales of ~ 1 km and less both along (Fig. 3, from ATM) and across (Fig. 4, from ICESat) the ice shelf. The ICESat tracks also reveal a deep channel near the middle of the ice shelf (Fig. 4). This channel coincides with the western track flown by aircraft surveys and is most pronounced in ICESat track 220, ~ 15 km seaward of the grounding line (Fig. 4). The elevation of this channel varies from a maximum of 18 m in November 2003 to minima of ~ 6 and ~ 8 m in March 2004 and March 2007, respectively (Figs 4 and 5). Linear trends from point measurements of elevation change over time are generally not significantly different from zero; however, the
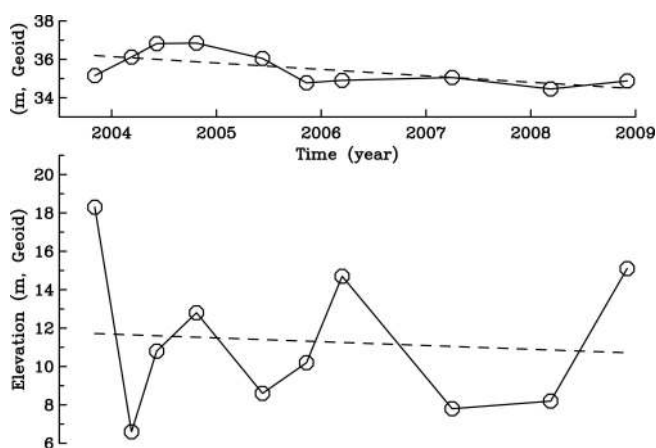

Fig. 5. ICESat-derived elevations for a segment of track 220 across PG as the mean elevation along 9 km of track (top panel) and minimum elevation (bottom panel) over the central section of the glacier (the segment of track 220 used for these averages is indicated in Fig. 4) as a function of time. Dashed lines indicate the linear trend that is significantly different from zero at 95% confidence for the averaged elevation $-0.33 \pm 0.26 \, \mathrm{m \, a^{-1}}$ (top) but not the minimal elevation $-0.20 \pm 1.5 \, \mathrm{m \, a^{-1}}$ (bottom).

along-track (approximately across-shelf) average over the central section of the surface elevation of the ice shelf decreased at a rate of $0.33 \pm 0.26 \, \mathrm{m \, a^{-1}}$ (Fig. 5); the uncertainty represents a 95% confidence limit in linear regression (Fofonoff and Bryden, 1975). This section includes both the central channel and the ambient ice shelf to its east and west.

The elevation of the ambient ice shelf on either side of the central channel is markedly different: the western ambient ice shelf stands 10–25% higher than the ambient ice shelf to the east. Along ICESat track 220, the time-mean, spatially averaged elevations are 33 and 31 m to the west and east of the central channel, with standard deviations of 6.0 and 11.7 m, respectively (Table 3). The elevation of the central channel is always less than half that of the nearby ambient ice shelf (cf. Rignot and Steffen, 2008).

We can trace the central channel seaward in ICESat tracks 101 and 1336, even though it becomes broader and its amplitude diminishes (Fig. 4; Table 3). The channel is also visible near the grounding line in ICESat track 339, and in MODIS imagery (Fig. 1). This observation allows us to use MODIS data (2000–12) to test whether the channel changes its lateral position during this period, which is longer than the ICESat period. Gradients of surface elevations cause variations in surface reflectance in remotely sensed optical MODIS imagery (Fig. 1). For similar Sun and satellite angles the spatial gradients of reflectance fall at similar locations (Scambos and others, 2007; Bindschadler and others, 2010). Figure 6 shows the absolute magnitude of the reflectance gradient vector for an across-shelf section located 15 km seaward of the grounding line near ICESat track 220. The central channel appears as a feature that does not move laterally by more than one pixel (250 m) throughout the 12 year record. It also reveals a distinct secondary peak gradient to the east of the central channel ($x \sim 83$ km), coincident with a shallower channel visible in ICESat elevation data (Fig. 4) ~ 4–5 km to the east of the central channel.

We further investigated elevation and ice-thickness change along ice flowlines using profiles from repeat ATM
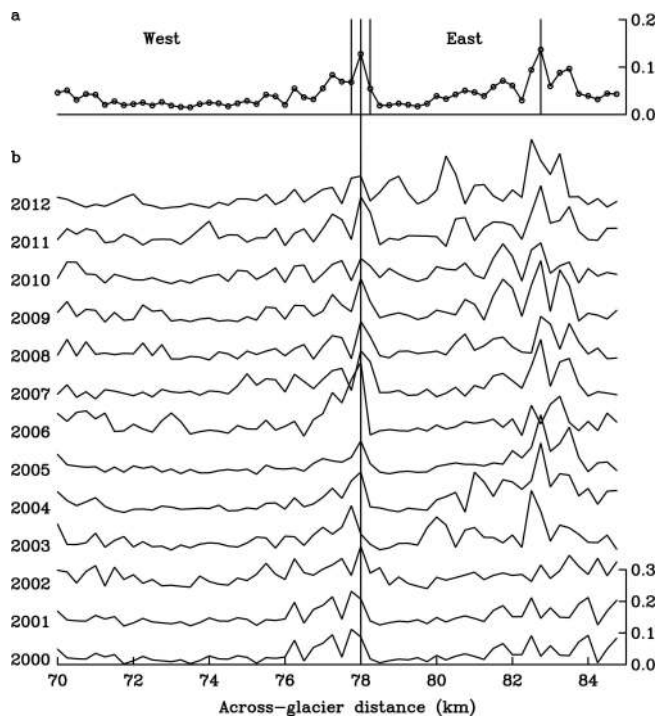
Fig. 6. Spatial gradients of surface reflectance derived from MODIS imagery across PG at $y = 15$ km (Fig. 1 shows location). (a) Average profile for 2000–12. (b) Reflectance profile by year. Vertical lines indicates the location of the central channel near $x = 78$ km with 250 m pixel size in (a) which also indicates a large secondary channel near $x = 82.75$ km.

surveys along the fjord, with two flight lines spaced 1.5 km apart. The ATM-derived elevation profile acquired in 2002 (Fig. 7) shows that the central (west) channel extends from the grounding line at least 50 km seaward and remains approximately half the thickness of the ambient ice shelf (east transect) for much of this range.

Ice draft and thickness profiles

We estimated along-ice-shelf draft from the ATM-derived elevations assuming hydrostatic equilibrium, and compared it with that estimated by ISR. For the ambient ice shelf, these two estimates show excellent agreement, with a correlation coefficient $r^2 = 0.993$. Figures 3 and 7 show these high correlations, which give confidence in the ice surface (ATM) and bottom (ISR) measurements as well as the validity of the hydrostatic assumption and the constant offset bias in Eqn (1) (Table 2). Deviations from hydrostatic equilibrium near the grounding zone indicate the location where the glacier sits on bedrock rather than being afloat (Fricker and others,

Table 3. Mean and standard deviation of ice thickness to the east and west of the central channel for ICESat sections. (Fig. 1 gives locations and Fig. 4 shows selected across-glacier thickness profiles)

Track	Years	Thickness east	Thickness west
		m	m
1336	6	16.5 ± 5.0	12.7 ± 4.6
101	7	23.0 ± 5.5	17.5 ± 6.2
220	10	33.4 ± 6.0	30.9 ± 11.7
339	9	87.2 ± 10.7	71.8 ± 11.7

2002; Bindschadler and others, 2011). Figure 7 suggests that the grounding zone is near 2 km in our coordinate system, consistent with the work of Rignot and Steffen (2008) based on 2002 and 2003 surface ground-penetrating radar data.

The same analysis applied to the 2002 transect along the central channel (Fig. 7c) shows similar agreement along most of the flight line; the exception is a ~5 km long region where the ISR-derived ice draft is much deeper than that derived from the ATM elevations assuming hydrostatic equilibrium. Based on ICESat track 220 across this region (Fig. 4), the minimum elevation in the central channel varies rapidly, from ~18 m in 2003 to ~6 m in 2004 (Fig. 5). This rapid change is consistent with advection of basal crevasses seen in the along-flowline transects of ice draft (Fig. 3). The ISR-estimated ice thickness is comparable with ice thickness of the ambient ice shelf at the same distance along the fjord; therefore, we tentatively interpret this region as a narrow basal channel that cannot be resolved by the ISR data, so the return echoes come from the ice base on either side of the channel. Given that the ice thickness in the channel (~150 m) is comparable with the width of the channel, it is also likely that the force balance for the ice across the channel is not fully hydrostatic but includes some bridging stresses, similar to an ice-shelf grounding zone (Fricker and Padman, 2006).

Ice-thickness change with time

Repeat-track analyses for ICESat track 220 (Figs 4 and 5), assuming general hydrostatic balance, suggest that the ice shelf is thinning at that location by 3.1 ± 2.4 m a^{-1}. If this thinning is applied to the 900 km^2 ice shelf in place after the 2012 calving, then it would account for 2.6 ± 2.0 Gt a^{-1} or ~20% of the total loss of mass from the 12 Gt a^{-1} crossing the grounding line.

The repeated flight lines in 2002, 2007 and 2010 allow us to determine the spatial extent of the ICESat-detected

Table 2. Petermann Gletscher ISR and ATM data. Date and regression parameters of ISR ice thickness and ATM elevations (offset$_i$ and ratio$_i$) along the central channel ($i = 1$) and along the ambient ice shelf ($i = 2$). Listed parameters are determined from data along a common 30 km long segment of floating ice shelf $y \in [21, 51]$ km. (Fig. 1 and Table 1 give locations)

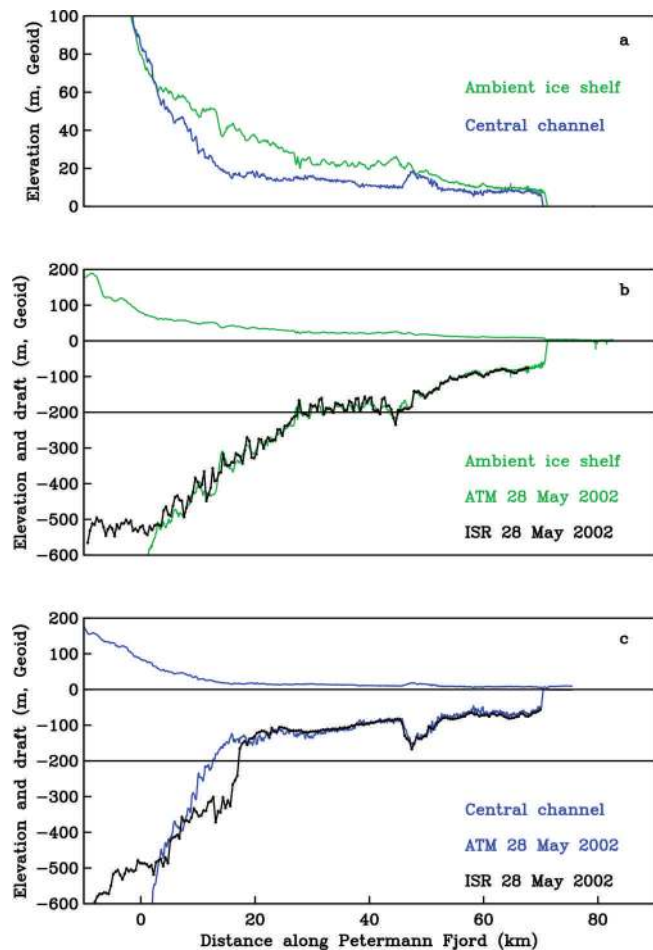| Date	offset$_1$	ratio$_1$	offset$_2$	ratio$_2$
	m		m	
24 Mar 2010	-4.0	0.131	$+0.5$	0.103
13 Sept 2007	-0.9	0.123	-0.0	0.115
14 May 2003	-1.1	0.127	$+1.2$	0.106

Fig. 7. Ice-shelf profiles of PG from ISR and ATM for 28 May 2002. (a) Surface elevation from ATM, (b) ambient ice shelf and (c) central channel. Vertical reference is the EGM2008 geoid. The ATM bottom traces are surface elevations scaled for hydrostatically floating ice.
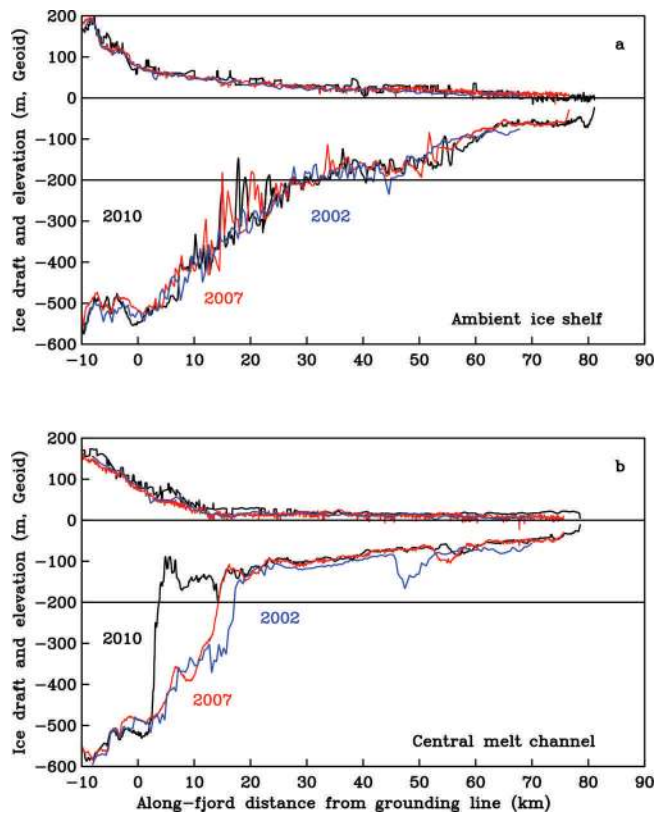

Fig. 8. ISR-derived ice draft and elevation along flowlines for (a) ambient ice shelf and (b) central melt channel for 2002, 2007 and 2010. Notice the retreat and steepening of the central melt channel from 2002 to 2010 towards the grounding line.

thinning. The repeats were always within 300 m of each other, with a root-mean-square deviation of 63 and 73 m for the track over the central channel and the ambient ice shelf, respectively (not shown). From the transects of MODIS surface reflectance gradients (Fig. 6), there was negligible lateral migration of the central channel during this period. The ISR-derived ice draft data show dramatic changes in the central channel within ~10 km of the grounding line between 2002 and 2010 (Fig. 8b); draft changed from 400 m in 2002 and 2007 to ~100–150 m in 2010. There was no discernible change on the ambient ice shelf, apart from the downstream migration of ~100 m high perturbations in the ice base (Fig. 8a).

We use the ISR ice thickness and corresponding ATM elevation data to quantify ice-thickness change along these flight lines. Using only surface elevation data from the ATM, we define an average ice thickness in hydrostatic equilibrium, $\widehat{H}$, as the integral from near the grounding line at $y_1 = 2$ km to some distance $y_2 > y_1$ along the ice shelf with $L = y_2 - y_1$:

$$\widehat{H}(x, t) = 1/L \int_{y_1}^{y_2} H(x, y, t)\, dy \qquad (2)$$

This reduces the noise of point-by-point elevation comparisons of a moving ice shelf with rough surface topography

such as PG (for other examples see Thomas and others, 2009; Schenk and Csatho, 2012).

Figure 9a and b show $H(y)$ and $\widehat{H}$, respectively, for the central channel and the ambient ice shelf for 2007 and 2010. Taking the 2012 terminus location as the limit, i.e. $y_2 = 48$ km, we find that the value of $\widehat{H}$ decreased from 216 m in 2007 to 203 m in 2010 over the central channel, and from 352 to 339 m on the ambient ice shelf over the same period (Fig. 9b; Table 4). We estimate that the floating ice shelf thinned by an average of 13 m along ice flowlines between 2007 and 2010. Note that the 2007 observations were taken in the summer after some seasonal surface melting had taken place, while the 2010 observations were taken in the spring when there was no surface melting. The actual time separation of the two profiles is 2.53 years.

Based on this comparison, the annual rate of hydrostatic thinning from 2007 to 2010 is 5.0 m a^{-1} for both the ambient ice shelf and the central channel. This corresponds to a surface lowering of ~0.53 m a^{-1} and is comparable to both the linear trend of ICESat across-shelf averaged elevation data of -0.33 ± 0.26 m a^{-1} for track 220 (Fig. 5; Table 4) and the regional value of -0.25 ± 0.06 m a^{-1} estimated by Gardner and others (2013) for all of north central Greenland.

DISCUSSION

The vertically averaged conservation of mass gives

$$\partial H / \partial t + \nabla(\vec{u}H) = \dot{a} - \dot{m}, \qquad (3)$$

where H is the ice thickness, $\vec{u} = (u, v)$ is the vertically averaged velocity vector with across- and along-stream
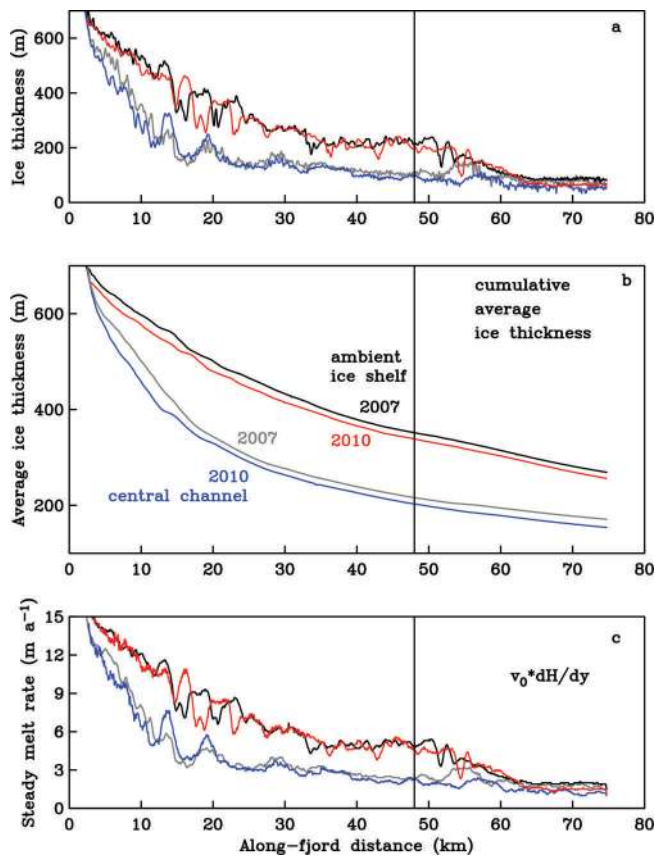
Fig. 9. ATM-derived ice-shelf profiles from PG for the central channel and ambient ice shelf surveyed in 2007 and 2010: (a) ice thickness, (b) cumulative average ice thickness and (c) ice flux divergence that in steady state corresponds to a melt rate. See Eqns (2) and (4) for details. In all graphs the central channel 2007 is the gray curve, central channel 2010 the blue curve, ambient ice shelf 2007 the black curve and ambient ice shelf 2010 the blue curve.

components u and v, $\dot{a}$ is the difference between surface ablation and accumulation ($\dot{a} > 0$ implies net accumulation) and $\dot{m}$ is the basal melt. The term $\nabla(\vec{u}H)$ can be rewritten as $\vec{u}\nabla H + H\nabla(\vec{u})$.

We first consider the steady-state mass balance, i.e. $\partial H/\partial t = 0$. Since the nonlinear dynamic thinning, $H\nabla\vec{u}$, is small (Higgins, 1991) and the across-stream flow is neg-

ligible, Eqn (3) simplifies to

$$v_0\, \partial H/\partial y = \dot{a} - \dot{m}, \qquad (4)$$

where v_0 is a constant along-stream velocity. Using this result, we estimate a net value of $\dot{a} - \dot{m}$ from thickness variations, H, along the ice shelf and $v_0 = 1.25\ \mathrm{km\,a^{-1}}$, based on feature tracking along repeat flight lines from 2010 to 2011 (Fig. 3). To calculate spatial gradients, we resampled the irregularly spaced ice-thickness profile into a constant along-glacier grid with $\delta y = 50\ \mathrm{m}$ spacing. This minimizes numerical artifacts when estimating the gradient, $\partial H/\partial y$, and net melt rate from Eqn (4).

The estimated net steady-state melt rate, $v_0\,\partial H/\partial y$, varies from $\sim 15\ \mathrm{m\,a^{-1}}$ near the grounding line to the surface ablation rate, $\dot{a} \simeq -1.2\ \mathrm{m\,a^{-1}}$, at the terminus (Fig. 9c). Averaging these values along each track for $y \in [2, 75]$ km in each year, we find almost identical net melt rates in 2007 and 2010, $\sim 4.9\ \mathrm{m\,a^{-1}}$ for the central channel and $\sim 8.0\ \mathrm{m\,a^{-1}}$ for the ambient ice shelf (Table 4). Across the 16 km wide ice shelf the central channel accounts for ~ 2 km; hence we partition the ice shelf into 1/8 central channel and 7/8 ambient shelf. Applying these weights to melt rates over the $900\ \mathrm{km^2}$ ice shelf in place after the 2012 calving, we attribute $6.3\ \mathrm{Gt\,a^{-1}}$ of ice loss to the steady-state term represented by divergence of the ice volume flux. This is only about half of the $12\ \mathrm{Gt\,a^{-1}}$ ice flux into the fjord at the grounding line (Rignot and Steffen, 2008); the remainder is provided by calving and non-steady thinning.

Between September 2007 and May 2010, the glacier thinned at a rate, $\partial\widehat{H}/\partial t$, of $5.0\ \mathrm{m\,a^{-1}}$ (Fig. 9b; Table 4). These values are of the same order of magnitude as the melt rates from the steady divergence (Eqn (4) and Fig. 9c). We thus conclude that PG's ice shelf was not in steady state prior to its extreme 2010 and 2012 calving events. The net melt rate is the sum of the non-steady and steady thinning,

$$\partial\widehat{H}/\partial t + v_0\sum_{k=1}^{N}\partial\widehat{H}(y_k)/\partial y = \dot{a} - \dot{m}, \qquad (5)$$

where $\partial H(y_k)/\partial y$ describes the thinning due to the ice divergence estimated along flowlines from 2007 and 2010 data (Fig. 9c). The net melt rate thus becomes $9.9\ \mathrm{m\,a^{-1}}$ for the central channel and $13.0\ \mathrm{m\,a^{-1}}$ for the ambient floating ice shelf. These values agree with those of Rignot and Steffen (2008) and Rignot and others (2001); however, we have

Table 4. ATM-derived mass-balance estimates of net melt rates ($\mathrm{m\,a^{-1}}$) averaged along two repeat flowlines near the central channel and the ambient shelf from Eqn (5) for the ice shelf to the 2012 terminus ($y \in [2, 48]$ km). The flux-gate estimates are from Rignot and others (2001) using radar interferometry and ATM data

	Year	$v_0\sum_k\partial H_k/\partial y$ $\mathrm{m\,a^{-1}}$	$\partial\widehat{H}/\partial t$ $\mathrm{m\,a^{-1}}$	Total $\mathrm{m\,a^{-1}}$	Thickness m
Central channel	2007	4.9			217
	2010	4.8			203
	2007–10	4.9	5.0	9.9	
Ambient shelf	2007	8.0			352
	2010	7.9			339
	2007–10	8.0	5.0	13.0	
ICESat-220	2003–09		3.1 ± 2.4		330
Flux-gate	1999	8.4	0.8	9.2	

shown that a significant fraction of this melting is from the non-steady component, $\partial H/\partial t$.

The melt rate maxima near the grounding line reach ~20 m a^{-1} in our calculations. These are ~20% smaller than those observed in 2002/03 by Rignot and Steffen (2008), who used the full velocity divergence, $\nabla(\vec{u}H)$, and the ice-thickness field measured by ice profiling ISR along ten along-glacier flight lines. In contrast, here we used hydro-static ice thickness derived from surface elevation ATM data along just two repeat lines. We hypothesize that the discrepancy arises because the ice shelf is not always in steady state at interannual timescales and not all regions of the ice shelf are in hydrostatic equilibrium, so that errors arise through interpreting surface elevation changes as hydrostatically compensated thickness changes.

We noted above that some sections of the along-flowline transects of ice draft show large basal crevasses (Figs 3 and 10). These crevasses are likely to be sufficiently small that they are not hydrostatically balanced. A section along the western wall of PG surveyed in 2011 revealed a sequence of eight to ten subsurface crevasses: ice thickness changes from 400 to 150 m within <500 m in the along-flow direction (Fig. 10). These undulations occur near the grounding line and do not have surface expressions. They appear similar in form to basal crevasses observed recently at Pine Island Glacier, Antarctica (Bindschadler and others, 2011; Vaughan and others, 2012), but have not previously been observed in North Greenland. Following Vaughan and others (2012), we hypothesize that stresses across these crevasses may contribute to structural weakening of the ice shelf. They may also impact basal melting; however, we do not know whether the net effect will be to increase or decrease mass loss by basal melting.

CONCLUSIONS

We have examined temporal variations of the Petermann Gletscher (PG) ice shelf in three dimensions for the decade leading up to the major calving events in 2010 and 2012, using available repeat-track airborne and ICESat laser altimeter data for the 2002–11 period and MODIS imagery for 2000–12. Following the 2012 calving event, the PG ice shelf was shorter than in any previous measurements since the first records from 1876. We find spatially averaged melt rates of 10–13 m a^{-1}, consistent with those reported by Rignot and Steffen (2008) and modeled by Gladish and others (2012). This rate includes a net thinning of 3–5 m a^{-1} during the 2003–10 period. The higher rates of 5 m a^{-1} are based on evolution of ice thickness during 2007–10, while the lower estimate is based on 2003–09 trends in elevation estimated by ICESat track 220, ~15 km north of the grounding line. Trends derived from ICESat tracks closer to the terminus are not significantly different from zero (not shown); however, the interannual variability of these esti-mates is larger and the sampling size is smaller, hence we cannot rule out linear trend values similar to those for ICESat track 220.

The role of ice-shelf basal channels and crevasses in net basal melting and ice-shelf structural integrity requires further exploration and modeling (Sergienko, 2013). Our analyses suggest similar rates of thinning in the central channel and the ambient ice shelf. This observation implies a greater fractional reduction rate in channels, where the ice is thinner, and raises the possibility that the weakening of ice in
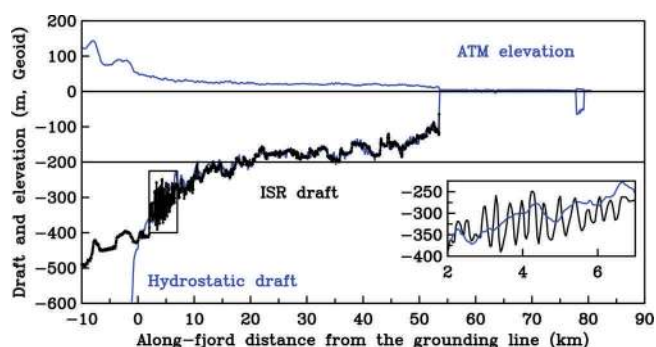

Fig. 10. Surface and basal elevation profiles along PG derived from ATM surface elevation (blue) and ISR (black) for 7 May 2011. The ATM-derived ice draft is based on ATM elevation assuming a hydrostatically floating ice shelf. The inset shows basal crevasses of ~150 m vertical excursion embedded in 400 m thick floating ice near the grounding line. Figure 1 shows the location of the inset.

the channels reduces the ability of the fjord's side-walls to constrain development of rifts that might be precursors to further large iceberg-calving events. We did not find any evidence of cross-fjord migration of channels in MODIS imagery for the period 2000–12 (Fig. 6), suggesting that basal melting within the channel does not occur preferentially to one side of the channel. Further interpretation is hampered by uncertainty in ice-thickness measurements from airborne radio-echo sounding across such narrow features, high-lighting the need for repeated surface ISR measurements and/or submarine profiling of ice-shelf basal topography (Vaughan and others, 2012; Stanton and others, 2013).

While the ice shelf of PG was not in steady state during the decade leading up to the large calving events in 2010 and 2012, we lack sufficient information to attribute its mass loss in this period to specific environmental changes. Rising subsurface ocean temperatures in adjacent Nares Strait (Münchow and others, 2011) may lead to warmer water entering the ocean cavity under the ice shelf of PG to increase basal melting. However, we cannot discount the potential role of atmospherically driven increases in summer surface meltwater runoff, either directly from the ice-shelf surface or as a basal freshwater flux across the grounding line from surface and basal melting further upstream. Large-scale ice-shelf retreat through calving also modifies the geometry of the fjord and, therefore, the thermohaline and atmospherically driven circulation of incoming warm water and outflowing upper-ocean cold, fresh water. Additional measurements and modeling are required to understand how projected changes in large-scale environmental condi-tions might impact the ocean/ice exchange processes within the fjord.

REFERENCES

Abshire JB and 7 others (2005) Geoscience Laser Altimeter System (GLAS) on the ICESat Mission: on-orbit measurement performance. *Geophys. Res. Lett.*, **32**(21), L21S02 (doi: 10.1029/2005GL024028)

Bamber JL, Siegert MJ, Griggs JA, Marshall SJ and Spada G (2013) Paleofluvial mega-canyon beneath the central Greenland ice sheet. *Science*, **341**(6149), 997–999 (doi: 10.1126/science.1239794)

Bindschadler RA, Scambos TA, Choi H and Haran TM (2010) Ice sheet change detection by satellite image differencing. *Remote Sens. Environ.*, **114**(7), 1353–1362 (doi: 10.1016/j.rse.2010.01.014)

Bindschadler R, Vaughan DG and Vornberger P (2011) Variability of basal melt beneath the Pine Island Glacier ice shelf, West Antarctica. *J. Glaciol.*, **57**(204), 581–595 (doi: 10.3189/002214311797409802)

Bjørk AA and 8 others (2012) An aerial view of 80 years of climate-related glacier fluctuations in southeast Greenland. *Nature Geosci.*, **5**(6), 427–432 (doi: 10.1038/ngeo1481)

Borsa AA, Moholdt G, Fricker HA and Brunt KM (2013) A range correction for ICESat and its potential impact on ice sheet mass balance studies. *Cryos. Discuss.*, **7**(4), 4287–4319 (doi: 10.5194/tcd-7-4287-2013)

Chen JL, Wilson CR and Tapley BD (2011) Interannual variability of Greenland ice losses from satellite gravimetry. *J. Geophys. Res.*, **116**(B7), B07406 (doi: 10.1029/2010JB007789)

Chylek P, Folland CK, Lesins G, Dubey MK and Wang M (2009) Arctic air temperature change amplification and the Atlantic Multidecadal Oscillation. *Geophys. Res. Lett.*, **36**(14), L14801 (doi: 10.1029/2009GL038777)

Falkner KK and 11 others (2011) Context for the recent massive Petermann Glacier calving event. *Eos*, **92**(14), 117–124 (doi: 10.1029/2011EO140001)

Fofonoff NP and Bryden H (1975) Density of sea waters. *J. Mar. Res.*, **41**, 69–82

Fricker HA and Padman L (2006) Ice shelf grounding zone structure from ICESat laser altimetry. *Geophys. Res. Lett.*, **33**(15), L15502 (doi: 10.1029/2006GL026907)

Fricker HA and 9 others (2002) Redefinition of the Amery Ice Shelf, East Antarctica, grounding zone. *J. Geophys. Res.*, **107**(B5), 2092 (doi: 10.1029/2001JB000383)

Fricker HA, Bassis JN, Minster B and MacAyeal DR (2005) ICESat's new perspective on ice shelf rifts: the vertical dimension. *Geophys. Res. Lett.*, **32**(23), L23S08 (doi: 10.1029/2005GL025070)

Fricker HA, Coleman R, Padman L, Scambos TA, Bohlander J and Brunt KM (2009) Mapping the grounding zone of the Amery Ice Shelf, East Antarctica using InSAR, MODIS and ICESat. *Antarct. Sci.*, **21**(5), 515–532 (doi: 10.1017/S095410200999023X)

Gardner AS and 15 others (2013) A reconciled estimate of glacier contributions to sea level rise: 2003 to 2009. *Science*, **340**(6134), 852–857 (doi: 10.1126/science.1234532)

Gladish CV, Holland DM, Holland PR and Price SF (2012) Ice-shelf basal channels in a coupled ice/ocean model. *J. Glaciol.*, **58**(212), 1227–1244 (doi: 10.3189/2012JoG12J003)

Gogineni S and 9 others (2001) Coherent radar ice thickness measurements over the Greenland ice sheet. *J. Geophys. Res.*, **106**(D24), 33 761–33 772 (doi: 10.1029/2001JD900183)

Higgins AK (1991) North Greenland glacier velocities and calf ice production. *Polarforschung*, **60**(1), 1–23

Holland DM, Thomas RH, De Young B, Ribergaard MH and Lyberth B (2008) Acceleration of Jakobshavn Isbræ triggered by warm subsurface ocean waters. *Nature Geosci.*, **1**(10), 659–664 (doi: 10.1038/ngeo316)

Howat IM, Joughin I, Fahnestock M, Smith BE and Scambos T (2008) Synchronous retreat and acceleration of southeast Greenland outlet glaciers 2000–2006: ice dynamics and coupling to climate. *J. Glaciol.*, **54**(187), 646–660 (doi: 10.3189/002214308786570908)

Howat IM, Ahn Y, Joughin I, Van den Broeke MR, Lenaerts JTM and Smith B (2011) Mass balance of Greenland's three largest outlet glaciers, 2000–2010. *Geophys. Res. Lett.*, **38**(12), L12501 (doi: 10.1029/2011GL047565)

Johannessen OM, Babiker M and Miles MW (2013) Unprecedented retreat in a 50-year observational record for Petermann Glacier, North Greenland. *Atmos. Ocean. Sci. Lett.*, **6**(5), 259–265 (doi: 10.3878/j.issn.1674-2834.13.0021)

Johnson HL, Münchow A, Falkner KK and Melling H (2011) Ocean circulation and properties in Petermann Fjord, Greenland. *J. Geophys. Res.*, **116**(C1), C01003 (doi: 10.1029/2010JC006519)

Joughin I, Abdalati W and Fahnestock MA (2004) Large fluctuations in speed on Greenland's Jakobshavn Isbræ glacier. *Nature*, **432**(7017), 608–610 (doi: 10.1038/nature03130)

Joughin I, Smith BE, Howat IM, Scambos T and Moon T (2010a) Greenland flow variability from ice-sheet-wide velocity mapping. *J. Glaciol.*, **56**(197), 415–430 (doi: 10.3189/002214310792447734)

Joughin I, Smith BE and Holland DM (2010b) Sensitivity of 21st century sea level to ocean-induced thinning of Pine Island Glacier, Antarctica. *Geophys. Res. Lett.*, **37**(20), L20502 (doi: 10.1029/2010GL044819)

Khan SA, Wahr J, Bevis M, Velicogna I and Kendrick E (2010) Spread of ice mass loss into northwest Greenland observed by GRACE and GPS. *Geophys. Res. Lett.*, **37**(6), L06501 (doi: 10.1029/2010GL042460)

Krabill WB (2010) *IceBridge ATM L1B Qfit elevation and return strength, Version 1.* NASA Distributed Active Archive Center, National Snow and Ice Data Center, Boulder, CO. Digital media: http://nsidc.org/data/ilatm1b.html

Krabill WB and 8 others (2002) Aircraft laser altimetry measurement of elevation changes of the Greenland ice sheet: technique and accuracy assessment. *J. Geodyn.*, **34**(3–4), 357–376 (doi: 10.1016/S0264-3707(02)00040-6)

Luckman A, Murray T, de Lange R and Hanna E (2006) Rapid and synchronous ice-dynamic changes in East Greenland. *Geophys. Res. Lett.*, **33**(3), L03503 (doi: 10.1029/2005GL025428)

Luo Y, Trishchenko AP and Khlopenkov KV (2008) Developing clear-sky, cloud and cloud shadow mask for producing clear-sky composites at 250-meter spatial resolution for the seven MODIS land bands over Canada and North America. *Remote Sens. Environ.*, **112**(12), 4167–4185 (doi: 10.1016/j.rse.2008.06.010)

Moon T, Joughin I, Smith B and Howat I (2012) 21st-century evolution of Greenland outlet glacier velocities. *Science*, **336**(6081), 576–578 (doi: 10.1126/science.1219985)

Motyka RJ, Truffer M, Fahnestock M, Mortensen J, Rysgaard S and Howat I (2011) Submarine melting of the 1985 Jakobshavn Isbræ floating tongue and the triggering of the current retreat. *J. Geophys. Res.*, **116**(F1), F01007 (doi: 10.1029/2009JF001632)

Münchow A, Falkner KK and Melling H (2007) Spatial continuity of measured seawater and tracer fluxes through Nares Strait, a dynamically wide channel bordering the Canadian Archipelago. *J. Mar. Res.*, **65**(6), 759–788 (doi: 10.1357/002224007784219048)

Münchow A, Falkner KK, Melling H, Rabe B and Johnson HL (2011) Ocean warming of Nares Strait bottom waters off northwest Greenland, 2003–2009. *Oceanography*, **24**(3), 114–123 (doi: 10.5670/oceanog.2011.62)

Nares G (1876) *The official report of the recent Arctic expedition.* John Murray, London

Nick FM and 8 others (2012) The response of Petermann Glacier, Greenland, to large calving events, and its future stability in the context of atmospheric and oceanic warming. *J. Glaciol.*, **58**(208), 229–239 (doi: 10.3189/2012JoG11J242)

Nick FM and 7 others (2013) Future sea-level rise from Greenland's major outlet glaciers in a warming climate. *Nature*, **497**(7448), 235–238 (doi: 10.1038/nature12068)

Padman L and Erofeeva S (2004) A barotropic inverse tidal model for the Arctic Ocean. *Geophys. Res. Lett.*, **31**(2), L02303 (doi: 10.1029/2003GL019003)

Padman L, Erofeeva SY and Fricker HA (2008) Improving Antarctic tide models by assimilation of ICESat laser altimetry over ice shelves. *Geophys. Res. Lett.*, **35**(22), L22504 (doi: 10.1029/2008GL035592)

Pavlis NK, Holmes SA, Kenyon SC and Factor JK (2012) The development and evaluation of the Earth Gravitational Model 2008 (EGM2008). *J. Geophys. Res.*, **117**(B4), B04406 (doi: 10.1029/2011JB008916)

Polyakov IV and 17 others (2010) Arctic Ocean warming contributes to reduced polar ice cap. *J. Phys. Oceanogr.*, **40**(12), 2743–2756 (doi: 10.1175/2010JPO4339.1)

Reeh N, Mayer C, Olesen OB, Christensen EL and Thomsen HH (2000) Tidal movement of Nioghalvfjerdsfjorden glacier, northeast Greenland: observations and modelling. *Ann. Glaciol.*, **31**, 111–117 (doi: 10.3189/172756400781820408)

Rignot E (1998) Hinge-line migration of Petermann Gletscher, north Greenland, detected using satellite-radar interferometry. *J. Glaciol.*, **44**(148), 469–476

Rignot E and Steffen K (2008) Channelized bottom melting and stability of floating ice shelves. *Geophys. Res. Lett.*, **35**(2), L02503 (doi: 10.1029/2007GL031765)

Rignot E, Gogineni S, Joughin I and Krabill W (2001) Contribution to the glaciology of northern Greenland from satellite radar interferometry. *J. Geophys. Res.*, **106**(D24), 34 007–34 019 (doi: 10.1029/2001JD900071)

Rignot E, Fenty I, Menemenlis D and Xu Y (2012) Spreading of warm ocean waters around Greenland as a possible cause for glacier acceleration. *Ann. Glaciol.*, **53**(60 Pt 2), 257–266 (doi: 10.3189/2012AoG60A136)

Scambos TA, Bohlander JA, Shuman CA and Skvarca P (2004) Glacier acceleration and thinning after ice shelf collapse in the Larsen B embayment, Antarctica. *Geophys. Res. Lett.*, **31**(18), L18402 (doi: 10.1029/2004GL020670)

Scambos TA, Haran TM, Fahnestock MA, Painter TH and Bohlander J (2007) MODIS-based Mosaic of Antarctica (MOA) data sets: continent-wide surface morphology and snow grain size. *Remote Sens. Environ.*, **111**(2–3), 242–257 (doi: 10.1016/j.rse.2006.12.020)

Schenk T and Csatho B (2012) A new methodology for detecting ice sheet surface elevation changes from laser altimetry data. *IEEE Trans. Geosci. Remote Sens.*, **50**(9), 3302–3316 (doi: 10.1109/TGRS.2011.2182357)

Sergienko OV (2013) Basal channels on ice shelves. *J. Geophys. Res.*, **118**(F3), 1342–1355 (doi: 10.1002/jgrf.20105)

Shuman CA and 6 others (2006) ICESat Antarctic elevation data: preliminary precision and accuracy assessment. *Geophys. Res. Lett.*, **33**(7), L07501 (doi: 10.1029/2005GL025227)

Stanton TP and 8 others (2013) Channelized ice melting in the ocean boundary layer beneath Pine Island Glacier, Antarctica. *Science*, **341**(6151), 1236–1239 (doi: 10.1126/science.1239373)

Straneo F and Heimbach P (2013) North Atlantic warming and the retreat of Greenland's outlet glaciers. *Nature*, **504**(7478), 36–43 (doi: 10.1038/nature12854)

Stroeve JC, Serreze MC, Holland MM, Kay JE, Malanik J and Barrett AP (2012) The Arctic's rapidly shrinking sea ice cover: a research synthesis. *Climatic Change*, **110**(3–4), 1005–1027 (doi: 10.1007/s10584-011-0101-1)

Thomas R, Frederick E, Krabill W, Manizade S and Martin C (2009) Recent changes on Greenland outlet glaciers. *J. Glaciol.*, **55**(189), 147–162 (doi: 10.3189/002214309788608958)

Trishchenko AP, Luo Y, Khlopenkov KV, Park WM and Wang S (2009) Arctic circumpolar mosaic at 250 m spatial resolution for IPY by fusion of MODIS/TERRA land bands B1–B7. *Int. J. Remote Sens.*, **30**(6), 1635–1641 (doi: 10.1080/01431160802348119)

Vaughan DG and 8 others (2012) Subglacial melt channels and fracture in the floating part of Pine Island Glacier, Antarctica. *J. Geophys. Res.*, **117**(F3), F03012 (doi: 10.1029/2012JF002360)

Wang M and Shi W (2009) Detection of ice and mixed ice–water pixels for MODIS ocean color data processing. *IEEE Trans. Geosci. Remote Sens.*, **47**(8), 2510–2518 (doi: 10.1109/TGRS.2009.2014365)

Wessel P (2009) A general-purpose Green's function-based interpolator. *Comput. Geosci.*, **35**(6), 1247–1254 (doi: 10.1016/j.cageo.2008.08.012)

Zweng MM and Münchow A (2006) Warming and freshening of Baffin Bay, 1916–2003. *J. Geophys. Res.*, **111**(C7), C07016 (doi: 10.1029/2005JC003093)